Nanoscale

ROYAL SOCIETY OF CHEMISTRY

PAPER

View Article Online
View Journal | View Issue

Cite this: *Nanoscale*, 2020, **12**, 16895

Direct nanofluidic channels *via* hardening and wrinkling of thin polymer films†

Jae Hyung Lee, Won Jun Chang, Won Young Choi, Jeong-Min Park, Jae-il Jang and Won Il Park *

Received 26th May 2020,
Accepted 28th July 2020

DOI: 10.1039/d0nr04032k

rsc.li/nanoscale

In this study, we propose a rational route to create wrinkling patterns with individually controllable location and direction in thin polymer films. Optical and atomic force microscopy analysis confirmed the formation of straight wrinkles with a typical width of 1.51 to 1.55 μm and a height of 60 to 65 nm. Confocal fluorescence microscopy revealed that each wrinkle produces a continuous hollow channel that interconnects neighboring holes in the polymer film, demonstrating potential applications as nanoscale fluidic channel and reactor. Moreover, we propose a mechanism that considers the elastic deformation energy and interface energies as crucial parameters that govern the mechanical instabilities, which provides scaling relationships between the height, width, and thickness of the wrinkles. This offers additional opportunities for control over the size and aspect ratio of the wrinkles and channels.

1. Introduction

Out-of-plane deformations frequently occur in thin sheets, such as human skin and artificial thin films. The resulting products, such as wrinkles, are often considered as an imperfection to be avoided. In spite of these negative views, there has been increasing interest in understanding the wrinkling mechanism and its potential applications.[1–12] Consequently, many approaches have been developed to generate and characterize wrinkles in thin sheets.[12–14] In particular, thin polymer sheets that are freestanding or adhered to more elastic substrates are the most frequently tested, and elastic energy minimization is commonly used to determine the mechanical instabilities. For example, Cerda *et al.* observed the development of a periodic array of winkles in a polyethylene sheet when it was subjected to uniaxial stretching beyond a critical strain.[15–18] Superimposed on the uniaxial stretching was the capillary force from a water droplet on a floating thin polymer film. In this case, wrinkles extend radially from the water droplet. The application of a buckling load is another common method of generating wrinkled structures. One example is when a stiff thin layer on a soft base, *e.g.*, a poly (dimethyl siloxane) sheet exposed to ultraviolet/ozone radiation under uniaxial stretching, is released to a stress-free state.[19–21] The resultant buckling yields a periodic or self-similar wrinkling pattern that is perpendicular to the stretching direction.

All the aforementioned studies provided an understanding of the winkling characteristics and revealed scaling relationships between the amplitude and wavelength of the wrinkles. However, most of these approaches are restricted to high density, uniaxial arrays of wrinkles.[19,22–30] Only a few groups including our own have developed approaches that can control the location and direction of each wrinkle in a thin membrane.[31–33] These approaches primarily utilize ordered networks of wrinkled-up nanochannels that are developed in periodically perforated thin films in a solution. In particular, Malachias *et al.* showed that wrinkles can be obtained from elastic and strained film (*e.g.*, InGaAs thin film on AlAs), which undergo stress and strain release during the etching of the sacrificial layers underneath.[31] The underlying mechanism of the experimentally observed nanochannel formation and the variation of nanochannel networks (*i.e.* the edge-to-diagonal-channel transition) were further analyzed theoretically by Annabattula *et al.*[33] Meanwhile, we found the wrinkling mechanism of a graphene-based thin membrane.[32] In our case, plastic deformation (*i.e.* elongation) of the thin membrane is induced by the trapped organic solvent, rather than the stress and strain release; subsequently, the gradual evaporation of the solvent through the periodical holes leads to wrinkle formation. The resulting wrinkles generally comprise a linear channel that interconnects the neighboring holes. We proposed a wrinkling mechanism analogous to the flattening and wrinkling that occur during wallpapering or ironing. Nevertheless, the complicated multilayer structures and fabrication processes have impeded the detailed understanding of

Division of Materials Science and Engineering Hanyang University, Seoul 04763, Republic of Korea. E-mail: wipark@hanyang.ac.kr

†Electronic supplementary information (ESI) available. See DOI: 10.1039/D0NR04032K

this phenomena. Herein, we further extend this strategy and propose a more rational route to enable wrinkling in monolayer polymer films. Atomic force microscopy (AFM) and confocal fluorescence microscopy unveil that each wrinkle produces a straight hollow channel. We consider not only elastic energy but also interface energy as crucial parameters that strongly influence the out-of-plane deformation. These energies, combined with quantitative assessments of the winkle structures, provide insight into the scaling relationships between the height, width, and thickness of the wrinkles.

2. Experimental

2.1. Fabrication of polymer wrinkles

Photoresist films with a 1.4 μm thickness were spun cast onto Si/SiO_2 substrates at 4000 rpm for 35 s and subsequently annealed at 95 °C for 1 min. Two-dimensional square arrays of holes, with diameters and center-to-center distances of 3 to 80 μm and 9 to 90 μm, respectively, were defined by photolithography. After exposure to a 60 W ultraviolet light for 18 s with a mask aligner (MIDAS MDA-400 M), the photoresist film was developed in a developer solution (AZ ELECTRONIC MATERIALS, AZ 300 MIF) for 15 s and rinsed with DI water.[38,39] The entire surface of the hole-patterned photoresist film was then treated with O_2 plasma in a vacuum chamber at 50 W for 70 s. This process hardened a thin layer, tens of nanometers thick, on the photoresist film. Subsequently, using a square plate as a shadow mask, the edges of the polymer film were exposed again to O_2 plasma for 90 s under the same conditions. The edge region exposed to the second plasma treatment became fully hardened, which acted as a clamp that held the thin polymer film during the subsequent wrinkling process. After the O_2 plasma treatment, the specimen was placed in an acetone solution for 20 min to remove the bottom layer of polymer film that remained unhardened and then rinsed with a methanol solution for 20 min. The specimen was then removed from the methanol solution and allowed to dry in air. As the trapped organic solution gradually evaporated through the holes, wrinkles that were interconnected with neighboring holes were generated.

2.2. Characterization

In situ observations of the wrinkling procedure, as well as investigations of the final structure, were conducted using an optical microscope (Olympus BX51). The shape and size of the polymer wrinkles were investigated by AFM (Park systems, XE-100) in the non-contact mode. The fluorescence microscopy images were obtained by a reflected laser scanning biological microscope (Olympus FV1200) using a short wavelength barrier filter (520–590 nm).

3. Results and discussion

Fig. 1a schematically shows the wrinkling process. It is noted that this approach uses a single layer polymer film, while a 4-layer film was needed in our previous work. This was achieved by (i) patterning the hole array, (ii) hardening the thin polymer film, and (iii) regulating the out-of-plane deformation in the film. First, a 1.4 μm thick photoresist film (AZ 5214a, pink color) with hole array defined *via* photolithography (Fig. 1a, I and II) was prepared. The film was then exposed to O_2 plasma (50 W, 70 s) which hardened a surface layer, tens of nanometers in thickness, on the photoresist film (Fig. 1a, III, dark brown color). The hardening was driven by plasma polymerization involving reactions between the O_2 gas phase species and polymer species that produced functional groups and crosslinking at the surface. The edge regions of the photoresist film were exposed again to O_2 plasma until the whole layer hardened (Fig. 1a, IV), which clamps the thin polymer films. Following the hardening process, the bottom layer of the photoresist film, which remained unhardened (soft), was removed *via* organic solvent etching and rinsing with acetone and methanol (Fig. 1a, V). The thin polymer film separated from the substrate but remained clamped by thick polymer film at the edges. When the specimen was removed from the methanol solution, the polymer film was floating on the organic solvent occupying the space between the film and substrate. Consequently, the trapped solvent evaporated gradually through the holes in the film. This resulted in buckling of the thin film, which produced straight wrinkles that were interconnected with neighboring holes (Fig. 1a, VI).

To elucidate the wrinkle formation process, *in situ* optical microscopy (OM) observations of the film with a square lattice of holes were performed immediately after removal from the solution (Fig. 1b and Mov. S1†). It was found that each midpoint between four adjacent holes first sank down and adhered to the surface of the substrate (dotted regions in Fig. 1b, t = 25 s). As time progressed, the adhered area spread, and wrinkle formation was recognized by the appearance of straight lines connecting the holes (Fig. 1b, $t \geq 40$ s). The final shape and size of the wrinkles was determined when the trapped solvent between the substrate and thin film was completely evaporated (Fig. 1b, t = 10 m). It is also worth noting that the polymer film remained unfixed in the absence of clamping around the edges, thereby producing an unregulated and random wrinkling pattern as well as a large in-plane distortion (Fig. S1†). However, when the edges of the film were clamped, only a small in-plane distortion was determined by the in-plane orientation of the wrinkles with a standard deviation of less than 1.8° (Fig. S2†).

In addition to the square lattice pattern, more discretionary patterns, such as a honeycomb lattice pattern, can be generated over a large area. Fig. 2a–c show the wrinkles that developed from a square lattice pattern with holes 3 μm in diameter and a 6 μm period (a, b), and a honeycomb lattice pattern with holes 10 μm in diameter and a 10 μm period (c). The straight wrinkles connecting neighboring holes show square (for the square lattice) and hexagonal shapes (for the hexagonal lattice). The dependence of the wrinkling phenomena on the hole diameter (D_h) was tested next. For instance, the number of wrinkles connecting the holes increases with D_h. Triplets

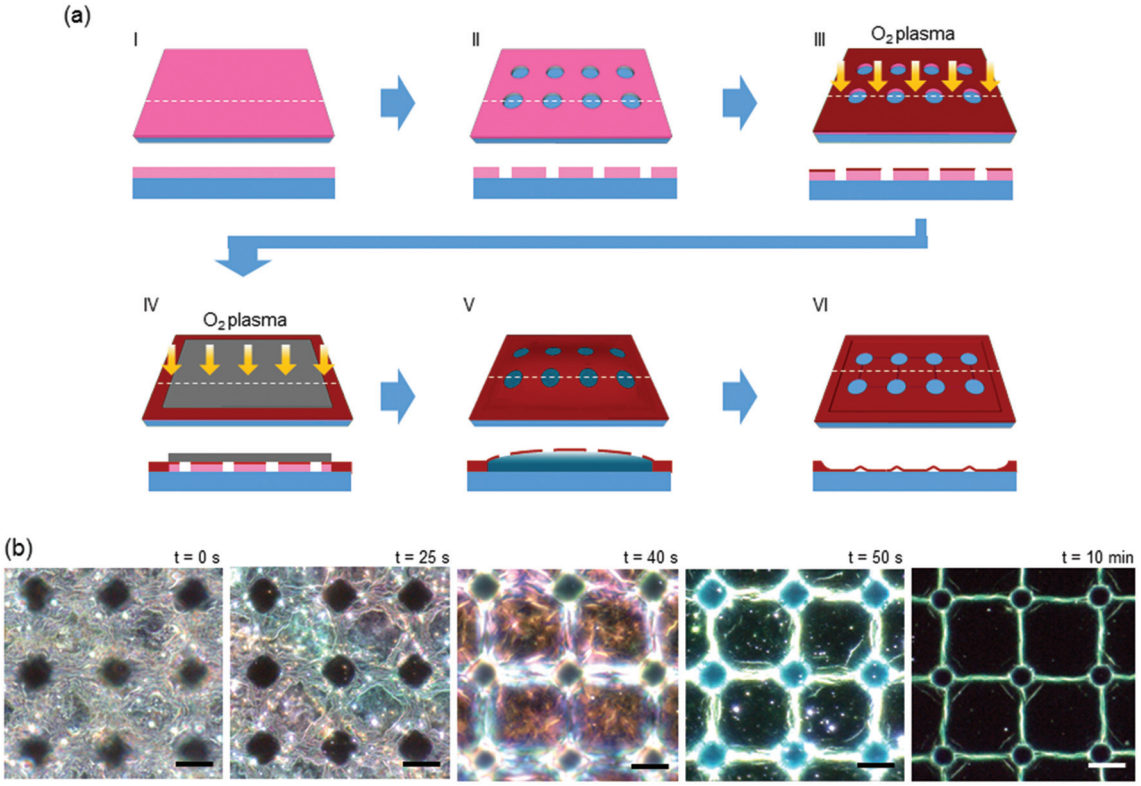

Fig. 1 Hardening and wrinkling of a thin polymer film. (a) Schematics of the overall process: patterning of the hole array (I and II), hardening (III and IV), and wrinkling (V and VI). Bottom panels: cross-sectional structures along the dashed lines in the top panels. Note that position of the dashed line in (VI) is different from those in (*I*–*V*). (b) *In situ* dark field microscopy images taken during wrinkling of a 25 nm thick polymer film from 0 to 10 min. Scale bars: 5 μm.

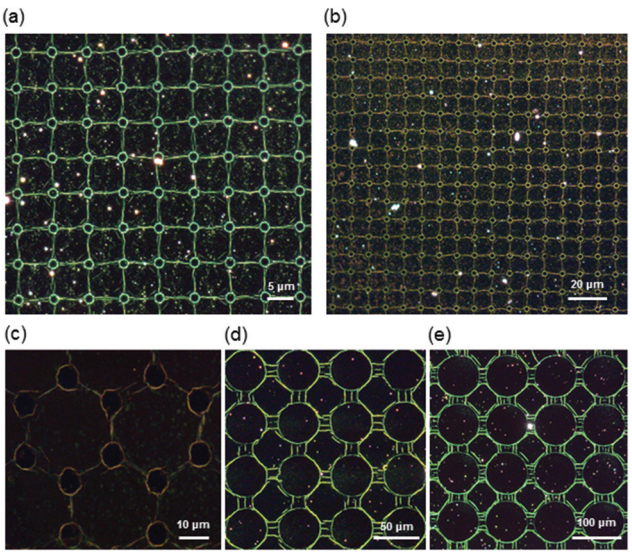

Fig. 2 Dark-field OM images of diverse wrinkle structures. (a–c) Wrinkles with (a, b) square and (c) honeycomb lattice patterns. The D_h/spacing are (a, b) 3/6 μm and (c) 10/10 μm, respectively. (d, e) Multiplets of wrinkles from the square lattice patterns for a D_h of (d) 40 and (e) 80 μm with an identical spacing between neighboring holes of ~10 μm.

and quadruplets of wrinkles formed from the square lattice patterns for D_h of 40 and 80 μm, respectively, with an identical spacing between neighboring holes of ~10 μm (Fig. 2d and e).

AFM analysis was performed for a more detailed analysis of the shape as well as the corresponding width and height of each wrinkle (Fig. 3a). The width to height ratio is larger for thinner polymer films. For 25 nm thick polymer films, the wrinkles have a gentle curve with a uniform width and height, typically 1.51–1.55 μm and 60–65 nm, respectively. It was confirmed that each wrinkle continuously interconnects the neighboring holes with no substantial break. In addition to the straight wrinkles interconnecting two adjacent holes, it was also found that circular wrinkles develop along the rim of each hole. Given the uniform thickness of the polymer film, this suggests that neighboring holes are connected by a straight, hollow, and unblocked channel in most cases (see also Fig. S3†).

To demonstrate the applicability of the wrinkles as nanofluidic channels, the wrinkles were filled with a solution containing a fluorescent dye.[20,30] A phosphate-buffered saline (PBS) solution containing 0.1 mol of Alexa Fluor 592 dye (Thermo fisher, wheat germ agglutinin, 5 mg) was used instead of the methanol solution in the last stage of wrinkling process (Fig. 1a, V). When the fluorescent dye-PBS solution on

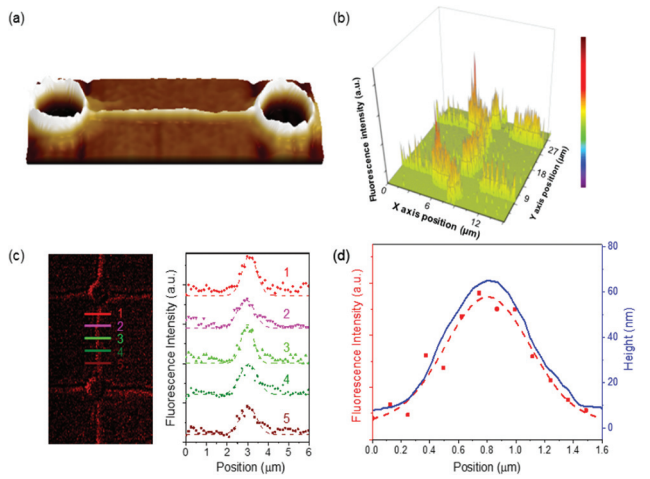

Fig. 3 Utilization of polymer wrinkles as nanofluidic channels. (a) 3D AFM image of wrinkle *via* analysis. (b) Position-dependent fluorescence intensity map showing the distribution of the fluorescent dye along the linear and circular wrinkles. (c) Fluorescence image and the cross-sectional profiles of the fluorescence intensity at five locations. (d) Overlap of fluorescence intensity (red dots and dashed line) and height profile of the wrinkle (blue line).

the outer surface of polymer film had completely evaporated, the sample was cleaned with purified water and then examined by a confocal microscope to investigate the distribution of the Alexa Fluor 592 dye. Position-dependent fluorescence intensity maps showed strong fluorescence along the linear wrinkles and the circular rims of holes (Fig. 3b). In addition, cross-sectional profiles of the fluorescence intensity at many locations have similar shapes and full width at half maximum (FWHM) values of 0.91 ± 0.13 with less than 15% variation (Fig. 3c). Importantly, the overlap of fluorescence intensity and height profile of the wrinkles shows that they have a similar intensity profile and width (Fig. 3d). This analysis indicates that most of the fluorescent dye molecules remain inside the wrinkles and suggests the potential application of these polymer wrinkles as nano/micro-scale fluidic channels. To better understand the wrinkling mechanism, an assessment of the dependence of the size and shape of the wrinkles on the design parameters and processing conditions is critical. Fig. 4a shows the geometry and defines the parameters used in this study: hole diameter (D_h), length (L), and width (W) of a unit segment marked by a white dashed square, film thickness (t), wrinkle height (H_w), wrinkle width (W_w), and elongated length (δL_w) of wrinkles compared with a flat surface. Given that the wrinkling is accompanied by an elongation of the film (that is, plastic deformation) involving the permeation and evaporation of the trapped solution, the ratio of δL_w of each wrinkle to L, which equals the center-to-center distance (D_{c-c}), was examined first. δL_w is obtained by the difference between the curved length calculated by a line integral and straight length of each wrinkle, which equals the W_w. Note that since it is somewhat ambiguous to determine W_w, W_w is defined as twice the FWHM measured from the Gaussian fitting of wrinkles. From this analysis, it was determined that δL_w is not dependent on L in the range of 20 to 90 μm (Fig. 4b, blue squares). The W_w and H_w, as well as their ratio, also exhibited a similar trend (Fig. 4b, red squares). This indicates that the elongation of the film is mostly determined by the final stage of evaporation of the solvent trapped between the buckled film and substrate surface. In this characterization, we confirmed that majority of the holes are completely interconnected by the wrinkles for the L value of up to 20 μm. However, the wrinkles do not completely connect the holes as the L increases to 30 μm; the wrinkles only form in the central regions between the holes. Furthermore, it was observed that the polymer films are easily torn around the holes as L increases above 50 μm, rather than developing wrinkle (Fig. S4 and S5†).

Accordingly, the final wrinkle structures, by considering the total free energy accompanying the out-of-plane deformation, can illuminate the wrinkling mechanism. To quantify the wrinkles, it is assumed that the exterior shape of each wrinkle sustains a single cycle of a sinusoidal waveform. This assumption is based on the fact that a parallel array of wrinkles is characterized as a multi-cycle sinusoidal wave in classical theory. Note that multiplets of wrinkles are also found for larger diameter hole patterns (*i.e.* $D_h > N{\cdot}W_w$, where N is the number of wrinkles in each hole). The corresponding elastic energy per unit area ($u_{elastic}$) accompanying the formation of wrinkle array with amplitude A and wavelength λ (corresponding to the W_w) scales as follows:[20,34–36] $u_{elastic} \approx E_p \cdot t^3 \cdot \left(\frac{A}{\lambda^2}\right)^2$, where E_p, which is associated with bending in a wrinkle of polymer, is the applied elastic modulus. For each wrinkle, H_w is twice of A, and W_w is equal to λ, so that $u_{elastic}$ can be rewritten: $u_{elastic} \approx E_p \cdot t^3 \cdot \left(\frac{2 \cdot H_w}{\lambda^2}\right)^2$. Given that each unit segment contains one wrinkle with a length of W, the elastic energy of a unit segment, $U_{elastic}$, scales as follows:

$$U_{elastic} \approx E_p \cdot t^3 \cdot \left(\frac{A}{\lambda^2}\right)^2 \cdot L \cdot W$$

Besides, contrary to more common wrinkling situations,[37] this case leads to a change in the interface energy per unit area, $u_{interface}$, as schematically shown in Fig. 4a. Considering the energies of the polymer-substrate interfaces (γ_{p-s}), polymer surface (γ_p), and substrate surface (γ_r), the interface energy of a unit segment, $U_{interface}$, is given by

$$U_{interface} = \gamma_{p-s} \cdot W \cdot (L - \lambda) + \gamma_p \cdot W \cdot (L - \lambda) + 2 \cdot \gamma_p \cdot W \cdot (\lambda + \delta L_w) + \gamma_s \cdot W \cdot \lambda$$

By adding the contribution of interface energies to the classical theory, the total free energy, U_{total}, can be given as:

$$U_{total} = E_p \cdot t^3 \cdot \left(\frac{2H_w}{\lambda^2}\right)^2 \cdot L \cdot W + [\gamma_{p-s} \cdot (L - \lambda) \cdot W + \gamma_p \cdot (L - \lambda) \cdot w + 2 \cdot \gamma_p \cdot (\lambda + \delta L_w) \cdot W + \gamma_s \cdot \lambda \cdot W$$

Meanwhile, to elucidate the contribution of t, the variation of t as a function of O_2 plasma exposure time was investigated

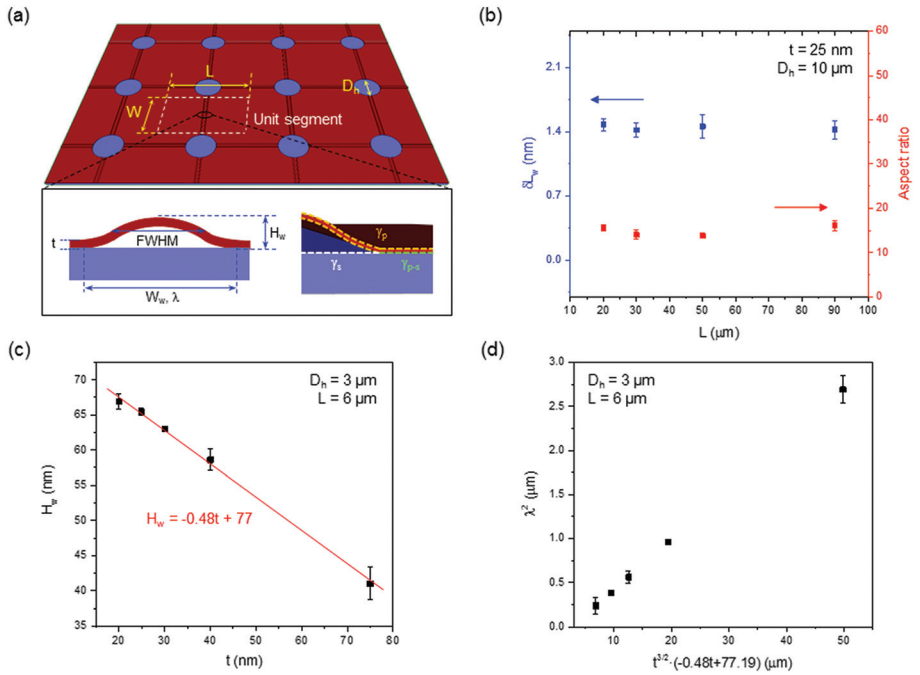

Fig. 4 Analysis of the wrinkles. (a) Schematic images of the wrinkle structure with geometry and definitions of the parameters: hole diameter (D_h), center-to-center distance (D_{c-c}), length (L) and width (W) of a unit segment, film thickness (t), wrinkle height (H_w), wrinkle width (W_w), elongated length (δL_w), polymer surface (γ_p), substrate surface (γ_s), and polymer-substrate (γ_{p-s}). (b) The δL_w (blue squares) and aspect ratio (red squares) as a function of L. (c) The relationship between H_w and t ($H = -0.48t + 77$) of wrinkles. (d) Plot of λ^2 *versus* $t^{3/2}\cdot(-0.48t + 77)$ of wrinkles.

(Fig. S6†). Then, further analysis of the dependence of H_w on t revealed that H_w decreases as t increases. Specifically, as is evident in Fig. 4c, the experimental data can be interpolated with a linear function: $H = -0.48\cdot t + 77$ for the case where D_h and L were fixed at 10 and 22 μm, respectively. In addition, given that λ is significantly larger than δL_w, the length of $\lambda + \delta L_w$ is close to λ. Minimizing U_{total} yields the following scaling law for wavelengths:

$$\lambda^2 = \left[\frac{3\cdot E_p}{-\gamma_{p-s}+\gamma_p+\gamma_s}\right]^{\frac{3}{2}}\cdot t^{\frac{3}{2}}\cdot(-0.48t+77)$$

The experimental values of λ^2 against $t^{3/2}\cdot(-0.48t + 77)$ are plotted in Fig. 4d, which show quantitative agreement with the scaling relationship. This validates the scaling law derived from both the elastic deformation energy and interface energy. This also predicts that an increase in t will lead to an increase in λ and a decrease in H_w, both of which contribute to a lower aspect ratio of the wrinkles. On the other hand, using a material with a smaller E_p would reduce λ and raise H_w, thus resulting in wrinkles with a higher aspect ratio. Similar contributions can be expected by improving the adhesion between the substrate and polymer or lowering γ_{p-s}.

To investigate whether the type of trapped solvent (or the evaporation rate) would affect the wrinkle formation, we characterized the wrinkles by changing the rinsing solution of methanol used in the last stage with acetone, ethanol, and isopropanol (steam pressures of acetone, methanol, ethanol and isopropanol solutions at 20 °C are 13.02 kPa, 24.6 kPa, 5.83 kPa, and 4.24 kPa, respectively). Despite the change in the evaporation rate, we determined that there are no detectable changes in the size and the network structure of the wrinkles (Fig. S7†). This result also supports the proposed wrinkling mechanism that considers the elastic deformation energy and interface energies of the final structures after complete evaporation of the trapped organic solvent.

4. Conclusions

In conclusion, we established a position- and direction-specific patterning of wrinkles in thin polymer films with a hollow channel inside. Based on *in situ* analysis of the wrinkling process and quantitative assessment of the final structures, a wrinkling mechanism, which considers the interface energies as another key parameter, was proposed. This analysis unveiled the scaling relationships between the height and width of the wrinkles and the film thickness, and suggested material considerations for additional control of the wrinkle structures. Thus, this study provides a new method to finely regulate the mechanical instability in various thin films, especially atomically thin materials, with many potential applications.

Conflicts of interest

There are no conflicts to declare.

Acknowledgements

This work was supported by the AFOSR/AOARD, USA (FA2386-18-1-4110) and the National Research Foundation of Korea funded by the Ministry of Science, ICT and Future Planning of Korea (No. 2018R1A2B2006410) and the Human Resources Program in Energy Technology of the Korea Institute of Energy Technology Evaluation and Planning (KETEP), granted financial resource from the Ministry of Trade, Industry & Energy, Republic of Korea (No. 20174030201750).

Notes and references

1 S. Yang, K. Khare and P.-C. Lin, *Adv. Funct. Mater.*, 2010, **20**, 2550–2564.
2 D. Chandra and A. J. Crosby, *Adv. Mater.*, 2011, **23**, 3441–3445.
3 H. S. Kim and A. J. Crosby, *Adv. Mater.*, 2011, **23**, 4188–4192.
4 M. Kato, T.-A. Asoh and H. Uyama, *Chem. Commun.*, 2019, **55**, 4170–4173.
5 H.-J. Park, C. Son and S.-H. Park, *Int. J. Precis. Eng. Manuf.*, 2014, **15**, 2469–2471.
6 P. J. Yoo and H. H. Lee, *Langmuir*, 2008, **24**, 6897–6902.
7 W. M. Choi, J. Song, D.-Y. Khang, H. Jiang, Y. Y. Huang and J. A. Rogers, *Nano Lett.*, 2007, **7**, 1655–1663.
8 Y.-A. L. Lee, V. Pryamitsyn, D. Rhee, M. O. de la Cruz and T. W. Odom, *Nano Lett.*, 2020, **20**, 1433–1439.
9 C.-M. Chen and S. Yang, *Polym. Int.*, 2012, **61**, 1041–1047.
10 A. R. Shugurov, A. I. Kozelskaya and A. V. Panin, *RSC Adv.*, 2014, **4**, 7389–7395.
11 H. Sasaki, H. Onoe, T. Osaki, R. Kawano and S. Takeuchi, *Sens. Actuators, B*, 2010, **150**, 478–482.
12 Y. Ebata, A. B. Croll and A. J. Crosby, *Soft Matter*, 2012, **8**, 9086–9091.
13 D. Wu, Y. Yin, F. Yang and H. Xie, *Appl. Surf. Sci.*, 2014, **320**, 207–212.
14 C. M. Stafford, C. Harrison, K. L. Beers, A. Karim, E. J. Amis, M. R. VanLandingham, H.-C. Kim, W. Volksen, R. D. Miller and E. E. Simonyi, *Nat. Mater.*, 2004, **3**, 545–550.
15 J. Chang, K. B. Toga, J. D. Paulsen, N. Menon and T. P. Russell, *Macromolecules*, 2018, **51**, 6764–6770.
16 B. Davidovitch, R. D. Schroll, D. Vella, M. Adda-Bedia and E. A. Cerda, *Proc. Natl. Acad. Sci. U. S. A.*, 2011, **108**, 18227.
17 J. Huang, M. Juszkiewicz, W. H. de Jeu, E. Cerda, T. Emrick, N. Menon and T. P. Russell, *Science*, 2007, **317**, 650.
18 K. B. Toga, J. Huang, K. Cunningham, T. P. Russell and N. Menon, *Soft Matter*, 2013, **9**, 8289–8296.
19 K. Efimenko, J. Finlay, M. E. Callow, J. A. Callow and J. Genzer, *ACS Appl. Mater. Interfaces*, 2009, **1**, 1031–1040.
20 K. Efimenko, M. Rackaitis, E. Manias, A. Vaziri, L. Mahadevan and J. Genzer, *Nat. Mater.*, 2005, **4**, 293–297.
21 J. Genzer and J. Groenewold, *Soft Matter*, 2006, **2**, 310–323.
22 W. Chen, X. Gui, B. Liang, M. Liu, Z. Lin, Y. Zhu and Z. Tang, *ACS Appl. Mater. Interfaces*, 2016, **8**, 10977–10984.
23 W.-B. Jung, K. M. Cho, W.-K. Lee, T. W. Odom and H.-T. Jung, *ACS Appl. Mater. Interfaces*, 2018, **10**, 1347–1355.
24 F. Zheng, Q. H. Thi, L. W. Wong, Q. Deng, T. H. Ly and J. Zhao, *ACS Nano*, 2020, **14**, 2137–2144.
25 E. P. Chan and A. J. Crosby, *Adv. Mater.*, 2006, **18**, 3238–3242.
26 J. Meng, J. Xie, X. Han and C. Lu, *Appl. Surf. Sci.*, 2016, **371**, 96–101.
27 Y. Yang, X. Han, W. Ding, S. Jiang, Y. Cao and C. Lu, *Langmuir*, 2013, **29**, 7170–7177.
28 N. Bowden, S. Brittain, A. G. Evans, J. W. Hutchinson and G. M. Whitesides, *Nature*, 1998, **393**, 146–149.
29 H. Vandeparre, S. Gabriele, F. Brau, C. Gay, K. K. Parker and P. Damman, *Soft Matter*, 2010, **6**, 5751–5756.
30 S. Chung, J. H. Lee, M.-W. Moon, J. Han and R. D. Kamm, *Adv. Mater.*, 2008, **20**, 3011–3016.
31 A. Malachias, Y. Mei, R. K. Annabattula, C. Deneke, P. R. Onck and O. G. Schmidt, *ACS Nano*, 2008, **2**, 1715–1721.
32 S. I. Lee, H.-G. Lim, S. S. Kwon, S. H. Kim, J. H. Lee, J.-M. Park, J.-I. Jang, S. I. Yang and W. I. Park, *Appl. Surf. Sci.*, 2020, **507**, 145184.
33 R. K. Annabattula and P. R. Onck, *Phys. Rev. B: Condens. Matter Mater. Phys.*, 2011, **84**, 054101.
34 T. Iwasa, *Int. J. Solids Struct.*, 2017, **121**, 201–211.
35 T. Iwasa, M. C. Natori and K. Higuchi, *J. Appl. Mech.*, 2004, **71**, 532–540.
36 E. Cerda, K. Ravi-Chandar and L. Mahadevan, *Nature*, 2002, **419**, 579–580.
37 D.-Y. Khang, J. A. Rogers and H. H. Lee, *Adv. Funct. Mater.*, 2009, **19**, 1526–1536.
38 J. H. Lee, W. W. Lee, D. W. Yang, W. J. Chang, S. S. Kwon and W. I. Park, *ACS Appl. Mater. Interfaces*, 2018, **10**, 14170–14174.
39 D. W. Yang, K. Lee, S. Jang, W. J. Chang, S. H. Kim, J. H. Lee, G.-C. Yi and W. I. Park, *J. Alloys Compd.*, 2019, **803**, 826–833.